Research Square

Preprints are preliminary reports that have not undergone peer review.
They should not be considered conclusive, used to inform clinical practice,
or referenced by the media as validated information.

An Elastoplastic Loading–Unloading Contact Model for Elliptical Paraboloidal Asperities with Lateral Interactions and Residual Deformation

Linbo Zhu
Xi'an Jiaotong University
Junbing Liu
Xi'an Jiaotong University
Rixin Qiu
Xi'an Jiaotong University
Junqi Zhou
Xi'an Jiaotong University
Jian Chen
jxfb0602@163.com
Xi'an Polytechnic University
Jun Hong
Xi'an Jiaotong University

Research Article

Keywords: Contact mechanics, Elliptical paraboloidal asperity, Loading-unloading, Residual deformation

Posted Date: June 10th, 2026

DOI: https://doi.org/10.21203/rs.3.rs-9870968/v1

License: This work is licensed under a Creative Commons Attribution 4.0 International License.
Read Full License

Additional Declarations: No competing interests reported.

An Elastoplastic Loading–Unloading Contact Model for Elliptical Paraboloidal Asperities with Lateral Interactions and Residual Deformation

Linbo Zhu[1], Junbing Liu[2], Rixin Qiu[1], Junqi Zhou[1], Jian Chen[3,] *, Jun Hong[2,] *

[1]: School of Chemical Engineering and Technology, Xi'an Jiaotong University, Xi'an 710049, China.

[2]: Key Laboratory of Education Ministry for Modern Design and Rotor-Bearing System, Xi'an Jiaotong University, Xi'an 710049, China.

[3]: School of Mechanical and Electrical Engineering, Xi'an Polytechnic University, Xi'an 710048, China

*: Corresponding Author

Email: jxfb0602@163.com (J. Chen), jhong@xjtu.edu.cn (J. Hong)

Abstract

Accurate modeling of asperity contact is essential for predicting friction, wear, and interface stiffness in mechanical systems. However, existing single-asperity models predominantly rely on simplified hemispherical or rotational paraboloidal geometries and assume purely normal interactions, thereby failing to capture the anisotropic and lateral contact behaviors inherent to real machined surfaces. In this work, an experimentally informed loading–unloading contact model is developed for laterally offset elliptical paraboloidal asperities with residual deformation. First, 3D topography measurements of AISI 1045 steel surfaces are analyzed using watershed segmentation, statistically demonstrating that the elliptical paraboloid better represents actual asperity geometry than the classical rotational paraboloid. Second, based on comprehensive finite element (FE) simulations covering various material properties and ellipticities, an empirical residual deformation model incorporating a shape parameter (λ) is established. This model expands the applicable loading range up to $300\omega_1$. Third, a complete elastoplastic unloading analytical framework is derived. By introducing a continuity-preserving correction factor, closed-form expressions for unloading loads are obtained. The proposed analytical model is validated against FE simulations, yielding a maximum error below 10%. Parametric analyses reveal two key findings: (i) tangential offset continuously modulates the contact stiffness throughout the entire loading–unloading cycle, and (ii) the anisotropic stress concentration unique to elliptical

paraboloids physically suppresses transverse expansion of plastic deformation. This model provides a high-fidelity micromechanical tool for tribological interface evaluations, particularly under conditions involving lateral misalignment and repeated contacts.

Keywords:

Contact mechanics; Elliptical paraboloidal asperity; Loading-unloading; Residual deformation

Nomenclature

a_i , b_i	Shape coefficients of the i-th asperity defining the two orthogonal principal curvatures
A,B	Combined curvature parameters
A_{e}	Contact area in elastic stage
A_{ep}	Contact area in elastoplastic stage
A_{p}	Contact area in fully plastic stage
$A(\lambda)$,$B(\lambda)$	Saturation upper limit coefficient and transition rate coefficient in the residual deformation empirical model
c_{A}	Material-dependent coefficient for initial yield
c_{h}	Hardness correction coefficient in the fully plastic state
c_{i}	Height constant of the iii-th asperity
d	Interference (vertical approach) between two asperities along the z-axis
E	Elastic modulus of asperity material
E^*	Equivalent elastic modulus of the two contact interfaces
H	Hardness of the softer material
k_{i1},k_{i2}	Two principal curvatures of the i-th asperity
K_v	Coefficient related to Poisson's ratio
m	Continuity-preserving correction factor
P_{e}	Contact load in elastic stage
P_{ep}	Contact load in elastoplastic stage
P_{p}	Contact load in fully plastic stage
$P_{\max}$	True maximum elastoplastic contact load at maximum deformation
$P_{\mathrm{ul,max}}$	Imaginary linear load at the simplified maximum deformation point C
$P_{\mathrm{ul}}(\omega)$	Unloading load as a function of normal deformation ω
r_x, r_y	Tangential offsets between the two asperities in the x and y directions

R_1, $R_1^{'}$	Two principal curvature radii of the upper asperity at the contact point
R_2, $R_2^{'}$	Two principal curvature radii of the lower asperity at the contact point
R_{m}	Equivalent radius of curvature at the contact point during loading
$R_m^{'}$	Equivalent radius of curvature during unloading under the simplified loading path
R_{mp}	Corrected equivalent radius of curvature during unloading
R_x, R_y	Two orthogonal principal radii of curvature of an elliptical paraboloidal asperity
$S(x,y)$	Surface roughness height matrix after preprocessing
ω	Normal deformation at the contact point
ω_1	Critical normal deformation marking the onset of elastoplastic deformation
ω_2	Critical normal deformation marking the onset of fully plastic deformation
$\omega_{\max}$	Maximum normal deformation reached during loading
ω_{res}	Residual normal deformation after complete unloading
x_{c},y_{c}	Coordinates of the contact point
δ	Interference between two asperities
λ	Shape parameter of elliptical paraboloid
υ	Poisson's ratio of asperity material
σ_y	Yield strength of asperity material

1 Introduction

In the assembly and operation of mechanical components, direct contact between mating surfaces has a decisive impact on the system's overall stability, sealing, and friction/wear performance [1-11]. At the microscopic scale, the contact of these interfaces essentially occurs between randomly distributed asperities (as shown in Fig. 1). Therefore, a deep understanding of the microscopic contact mechanical behavior of a single asperity is the foundation and key to constructing constitutive models for macroscopic interfaces.

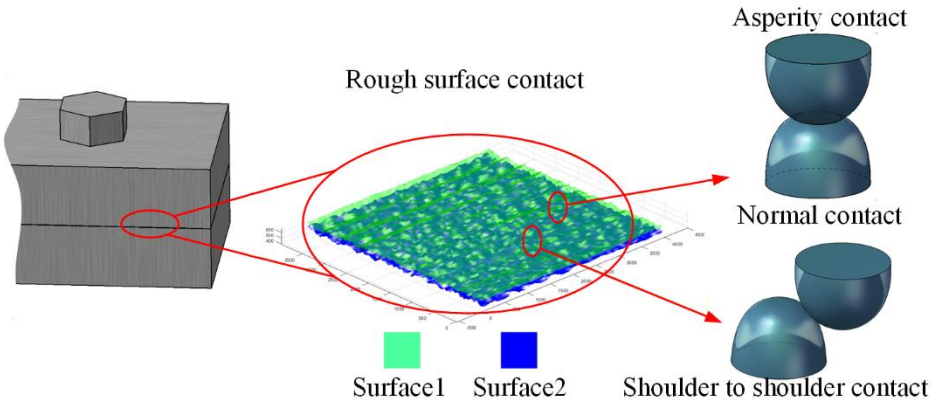


Fig. 1. Engineering surface and its asperities.

For over half a century, researchers have conducted extensive and in-depth studies on the contact behavior of asperities. Greenwood and Williamson [12] were the first to propose the GW model, which describes the fully elastic contact of rough surfaces based on Hertz theory. Since this model only considers elastic deformation, Chang et al. [13] established the CEB elastoplastic contact model based on the volume conservation hypothesis. Subsequently, Zhao et al. [14] further developed a contact model with smooth transitions connecting the elastic and fully plastic stages. With the popularization of the finite element method, Kogut and Etsion [15] established the classic frictionless hemispherical elastoplastic contact FE model (the KE model), while Jackson and Green [16] proposed the JG model by considering the hardness change caused by contact geometric deformation. In recent years, researchers have further explored the influence of the friction coefficient, strain hardening parameters, and material properties on the contact characteristics of asperities under loading [17-19]. However, these classic models mainly focus on the forward loading process and are all based on the idealized "hemispherical" asperity geometric assumption.

Mechanical operation is frequently accompanied by load fluctuations and surface separation; therefore, the unloading behavior of asperities is equally critical for evaluating the lubrication, sealing, and long-term service of tribological interfaces [20-23]. Vu-Quoc et al. [24] first proposed a simple theoretical model for the normal loading and unloading of elastoplastic spheres. Subsequently, Etsion et al. [25] conducted systematic FE simulations on the unloading process of hemispherical asperities and provided dimensionless empirical formulas for predicting the residual interference and residual curvature after complete unloading (the classic KE unloading model). On this basis, Zhao et al. [26] corrected the influence of the tangent modulus on unloading laws;

recently, Chen, Luo, et al. [27-29] further investigated the loading and unloading mechanical behavior under strain hardening, yield plateaus, and large deformation depths. It must be emphasized that existing empirical models for residual deformation are almost entirely limited to standard spherical asperities and fail to reflect the influence of geometric anisotropy.

Real machined surfaces have complex topography, and equating asperities simply to isotropic hemispheres has significant limitations [30-33]. To more accurately characterize real surface morphology, researchers have introduced the concept of ellipticity to expand contact theory. Based on experimental results, Jamari and Schipper [34] derived a semi-analytical loading model for the elastoplastic contact of anisotropic ellipsoids. Lin and Lin [35] analyzed the influence of ellipticity on critical interference through finite element analysis. In recent years, Chen et al. [36, 37] and Wen et al. [38, 39] explored the normal loading and unloading behavior of ellipsoidal asperities against rigid planes; Becker and Kamlah [40] proposed a force-deformation relationship model for normal contact loading and unloading, targeting non-spherical objects like lithium-ion battery particles. Nevertheless, the vast majority of these anisotropic models remain limited to "purely normal centered" contact between the asperity vertex and a rigid plane.

In real assembly interfaces, due to the random spatial distribution of asperities on upper and lower surfaces, the two opposing asperities rarely engage in ideal vertex-to-vertex contact; instead, lateral contact, where there is a tangential spatial offset, dominates. Addressing this, Peng et al. [41] proposed a constriction resistance model for rough surfaces considering lateral contact; Zhou et al. [42] applied this to the contact analysis of gear tooth surfaces; Wang [41] and Fan et al. [43] have also recently established analytical models for lateral contact that consider the horizontal distance distribution of asperities. Despite these positive developments, existing research on lateral contact still faces obvious limitations: first, most models continue to use the hemispherical assumption, ignoring the coupling effect between real morphology anisotropy and lateral contact; second, research remains stuck in the elastic or loading stages, rarely involving the elastoplastic unloading process, and lacks quantitative analysis of permanent residual deformation after unloading.

In summary, there are three key research gaps in the current field of asperity contact mechanics: (1) The widely adopted hemispherical and anisotropic asperity geometric

assumptions lack quantitative verification based on real machined surface statistical data; (2) Classic empirical residual deformation models (such as the KE model) are limited by spherical geometry, fail to reflect the influence of morphology parameters, and their applicability in large deformation ranges has not been fully extended; (3) For the more common lateral contact configuration in engineering, there is currently a lack of a complete closed-form unloading solution that includes both the anisotropy of elliptical paraboloids and elastoplastic residual deformation.

To fill these theoretical gaps, this paper carries out the following three innovative tasks: First, high-precision confocal microscopy is used to perform 3D topography measurement and watershed segmentation identification on ground, milled, and turned AISI 1045 steel surfaces, quantitatively verifying the superiority of the elliptical paraboloid model in representing real asperity morphology from a statistical perspective. Second, based on large-scale finite element contact simulation data, an empirical residual deformation model incorporating a shape parameter is established, which, for the first time, extends the classic unloading model to elliptical paraboloid geometry and expands its applicable loading range to $300\omega_1$. Third, an analytical mechanical framework for the loading and unloading of laterally contacting elliptical paraboloids—including geometric morphology parameters and tangential offsets—is established, and a closed-form analytical formula for elastoplastic unloading loads is derived by introducing a continuity-preserving correction factor. The model proposed in this paper has been validated through finite element analysis under various working conditions, aiming to provide a microscopic mechanical tool closer to real physical states for predicting the evolution behavior and contact stiffness of tribological interfaces.

2 Geometric Characterization of Real Surface Asperities

To establish a realistic geometric foundation for the contact model, the three-dimensional topographies of ground, milled, and turned AISI 1045 steel surfaces were acquired using a confocal laser scanning microscope (4000 μm × 4000 μm area, 1 μm lateral resolution). The raw data were preprocessed via reference plane fitting for tilt correction and bior3.7 wavelet filtering for noise removal. Individual asperities were then identified using watershed segmentation combined with an 8-nearest-neighbor region merging strategy to eliminate over-segmentation [44-47], as illustrated in Fig. 2.

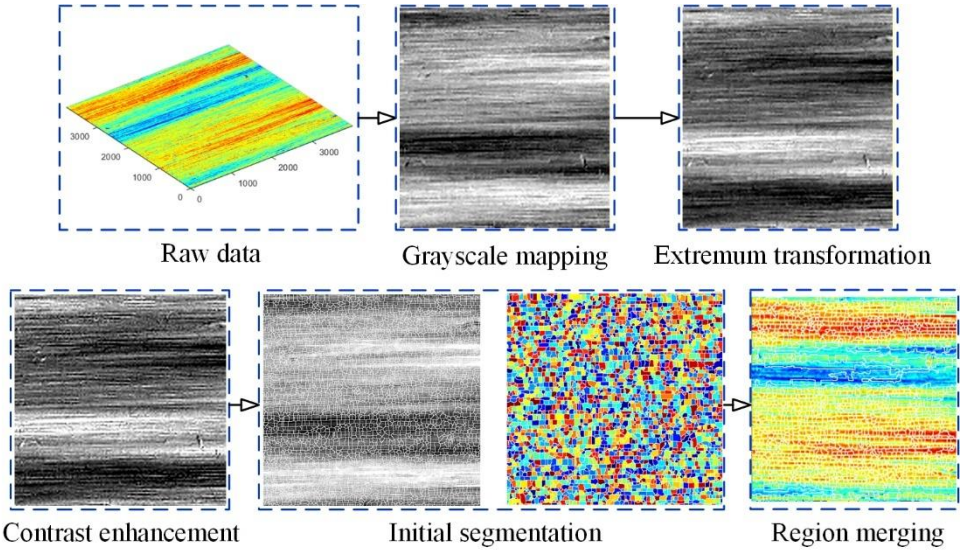


Fig. 2. Watershed processing workflow.

In classic contact mechanics frameworks, asperities are usually highly idealized as isotropic Rotational Paraboloids. However, real machining processes leave significant machining textures on the surface, causing asperities to exhibit strong directionality and anisotropy. To explore the geometric model that best fits the real physical morphology, this section uses the extracted asperity region data to perform surface fitting and error comparison for rotational paraboloids and elliptical paraboloids, respectively.

For the rotational paraboloid model, its geometric equation is constrained to Eq.(1), requiring the radii of curvature in two orthogonal directions to be identical. However, the elliptical paraboloid model equation proposed in this paper is Eq.(2), allowing for two independent principal radii of curvature.

$$z_{\mathrm{R}}\left(x,y\right)=a_{\mathrm{R}}\left(x^{2}+y^{2}\right)+c_{\mathrm{R}} \tag{1}$$

$$z_{\mathrm{E}}\left(x,y\right)=a_{\mathrm{E}}x^{2}+b_{\mathrm{E}}y^{2}+c_{\mathrm{E}} \tag{2}$$

During the fitting process, with the identified rough peak vertex as the initial center, the Levenberg-Marquardt algorithm is used to independently optimize within the segmented boundary of each asperity. To quantitatively evaluate the fidelity of these two geometric models to the real topography, the root mean square error (RMSE), mean absolute error (MAE), and coefficient of determination (R^2) were calculated for all identified asperity samples.

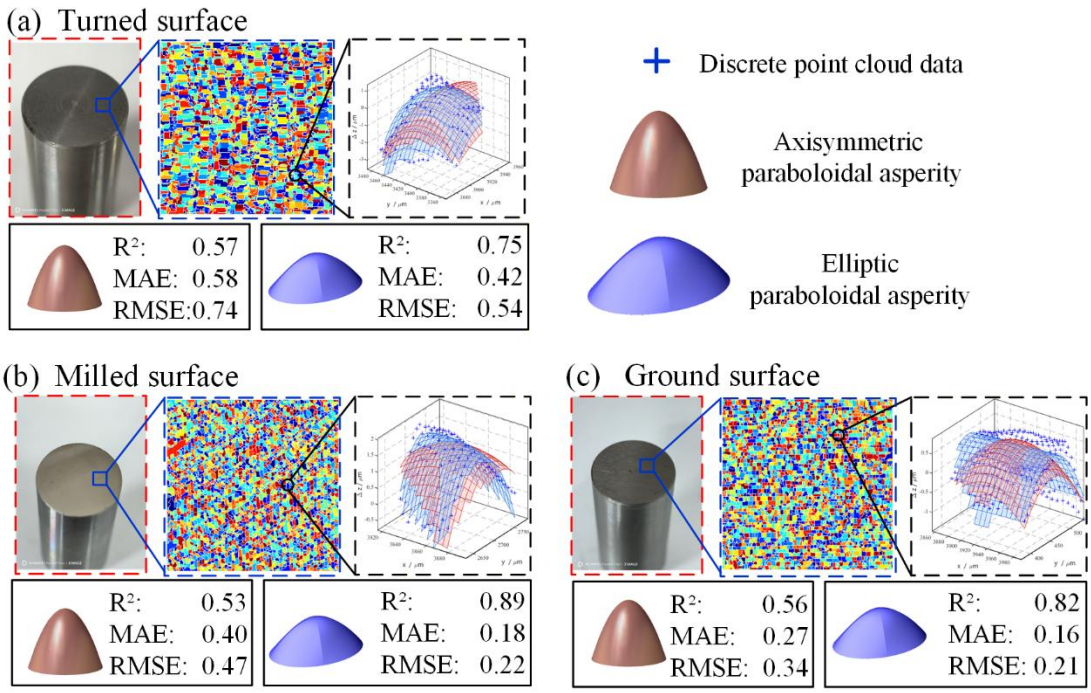


Fig. 3. Comparison of fitting evaluation metrics for hemispherical and elliptical paraboloidal asperity geometric models for different machined surfaces.

Fig. 3 shows the statistical distribution comparison of fitting evaluation indicators for asperity samples under three machined surfaces. It can be clearly observed that for ground, milled, and turned surfaces, the coefficient of determination R^2 of the elliptical paraboloid model is significantly higher than that of the rotational paraboloid model, meanwhile, its RMSE and MAE error indicators have significantly decreased. The geometric essence of this significant difference is that the rotational paraboloid, limited by its inherent axial symmetry assumption, is forced to share a single curvature in both the x and y orthogonal directions, which completely masks the anisotropic features caused by cutting marks on real machined asperities. When facing elongated or spindle-shaped asperities, the rotational paraboloid usually has to compromise on an intermediate average curvature, leading to huge spatial deviations in the main axis edge regions. In contrast, the elliptical paraboloid model releases shape constraints and can independently adjust two principal radii of curvature with high degrees of freedom, thereby capturing the morphological evolution of asperities in different orthogonal directions with high fidelity. This statistical comparison based on measured surface data fully exposes the limitations of the rotational paraboloid assumption when characterizing machined surfaces. It not only quantitatively proves the scientific nature of the elliptical paraboloid as a fundamental geometric form for microscopic contact

but also provides a solid, irrefutable physical basis for subsequently introducing the shape parameter λ to construct an accurate loading-unloading contact model for anisotropic lateral contacts.

3 Lateral Contact Framework for Elliptical Paraboloidal Asperities

Real tribological interface contact does not always occur at the center of the asperity. Due to the random spatial distribution of microscopic topography, the lateral contact mode dominates, characterized by a tangential offset between asperity pairs. This section establishes the contact geometric configuration between two elliptical paraboloid asperities under tangential offset. Based on this, the classic anisotropic loading contact theory is extended to the lateral contact mode, providing the necessary analytical framework and state variables for establishing the residual deformation model and the elastoplastic unloading closed-form solution.

3.1 Geometric Configuration and Contact Area

Consider the lateral contact occurring between two elliptical paraboloid asperities with independent curvatures, as shown in Fig. 4. In a unified local Cartesian coordinate system, assume the vertex of the lower asperity is located at the origin, the upper asperity has tangential offsets r_x and r_y in the horizontal direction, and an interference δ in the vertical (z-axis) direction. At this time, the surface morphology equations of the upper and lower asperities can be expressed as:

$$z_1(x,y) = a_1(x-r_x)^2 + b_1(y-r_y)^2 + c_1 - \delta \tag{3}$$

$$z_2(x,y) = a_2x^2 + b_2y^2 + c_2 \tag{4}$$

where a_i and b_i are the shape coefficients representing the two orthogonal principal curvatures of the i-th asperity, and c_i is the height constant (i=1,2).

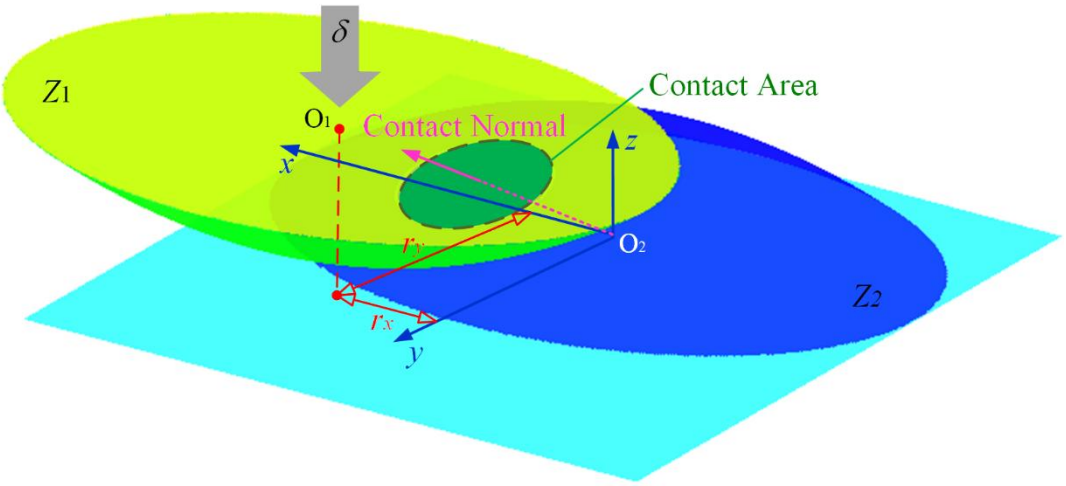


Fig. 4. General form of lateral contact between two elliptical paraboloid asperities.

For complex non-centered anisotropic contact, solving for its actual principal curvatures usually requires using the first and second fundamental forms of the surface to solve the eigenvalue problem. To keep the main thread of the text compact, the specific algebraic derivation process for contact point coordinates (x_c, y_c), the contact surface normal vector, and its principal curvatures is included in full in Appendix A. The equivalent radius of curvature R_{m} at the contact point for this lateral contact configuration can be expressed as:

$$R_{\mathrm{m}} = \frac{1}{R_x} + \frac{1}{R_y} = \frac{1}{R_1} + \frac{1}{R_1'} + \frac{1}{R_2} + \frac{1}{R_2'} \tag{5}$$

where R_1 and $R_1^{'}$ are the two principal curvature radii of the upper asperity at the contact point, while R_2 and $R_2^{'}$ are the two principal curvature radii of the lower asperity, with these latter values being the reciprocals of the principal curvature κ.

3.2 Contact Constitutive at the Loading Stage

(Author's statement: The elastoplastic contact constitutive expression adopted in this section mathematically inherits and extends the elliptical ellipsoid forward contact framework proposed by Jamari and Schipper [34]. The contribution of this paper is to explicitly introduce the equivalent radius of curvature Rm, which includes the effect of tangential offsets (r_x, r_y), into this framework to achieve accurate assessment of anisotropic lateral contact and establish the load-displacement initial boundaries for the unloading closed-form solution containing residual deformation derived in section 5.)

As the normal deformation δ increases, the asperities in lateral contact will experience three deformation stages in sequence: fully elastic, elastoplastic, and fully plastic. The critical deformation and constitutive relationship for each stage are as

follows:

(1) Fully Elastic Stage ($\delta \leq \delta_1$)

In the early stage of deformation, contact behavior follows the classic Hertz contact theory. The critical normal deformation w1 for elastic contact is defined as the moment when the material begins to yield, expressed as:

$$\delta_1 = \frac{\pi^2}{2}\alpha^2\beta^2\gamma R_{\mathrm{m}}\frac{K_v^2 H^2}{E^2\cos\theta} \tag{6}$$

where H is the hardness of the softer material, E is the equivalent elastic modulus of the two contact interfaces, and K_{v} is a coefficient related to Poisson's ratio and can be determined from equation [34]:

$$K_v = 0.454 + 0.41v \tag{7}$$

In this stage, the actual contact area A_{e} and contact load P_{e} are:

$$A = 2\pi R_{\mathrm{m}}\frac{\alpha\beta}{\gamma}\delta\cos\theta \tag{8}$$

$$P = \frac{4\sqrt{2}}{3}ER_{\mathrm{m}}^{0.5}\left(\frac{\delta\cos\theta}{\gamma}\right)^{1.5} \tag{9}$$

(2) Fully Plastic Stage ($\delta \geq \delta_2$)

When normal deformation further increases and exceeds the fully plastic critical deformation δ_2, the entire contact region enters a state of full plastic flow. The expression for critical point δ_2 is:

$$\delta_2 = \delta_1 c_{\mathrm{A}}\frac{R_{\mathrm{m}}}{\sqrt{R_x R_y}}\frac{\alpha\beta}{\gamma} \tag{10}$$

where c_{h} is the hardness correction coefficient in the fully plastic state. After entering this stage, the contact area A_{p} and load P_{p} evolve as:

$$A_{\mathrm{p}} = 2\pi\sqrt{R_x R_y}\delta\cos\theta \tag{11}$$

$$P_{\mathrm{p}} = 2\pi\sqrt{R_x R_y}c_{\mathrm{h}}H\delta\cos\theta \tag{12}$$

(3) Elastoplastic Transition Stage ($\delta_1 < \delta < \delta_2$)

The contact area A_{ep} and contact load P_{ep} in the elastoplastic stage can be expressed as:

$$A_{\mathrm{ep}}=\left(2\pi\sqrt{R_xR_y}\delta\cos\theta-2\pi R_{\mathrm{m}}\frac{\alpha\beta}{\gamma}\delta\cos\theta\right)\left[3\left(\frac{\delta-\delta_1}{\delta_2-\delta_1}\right)^2-2\left(\frac{\delta-\delta_1}{\delta_2-\delta_1}\right)^3\right]+2\pi R_{\mathrm{m}}\frac{\alpha\beta}{\gamma}\delta\cos\theta \tag{13}$$

$$P_{\mathrm{ep}}=A_{\mathrm{ep}}H\left[c_{\mathrm{h}}-\frac{\ln\delta_2\cos\theta-\ln\delta\cos\theta}{\ln\delta_2\cos\theta-\ln\delta_1\cos\theta}\left(c_{\mathrm{h}}-\frac{2}{3}K_v\right)\right] \tag{14}$$

4 Elastic-Plastic Unloading Contact Model with Shape-Dependent Residual Deformation

In real tribological interfaces, asperity contact is often accompanied by periodic fluctuations in normal load and surface separation. Therefore, deriving the elastoplastic unloading load-displacement relationship for asperities has important engineering significance. Mechanically, because elastoplastic deformation is irreversible, the unloading path is highly dependent on the location of the unloading endpoint. This section first establishes an empirical residual deformation model suitable for anisotropic elliptical paraboloids based on a large amount of finite element simulation data; subsequently, it returns to the analytical mechanics framework and derives a closed-form solution for the unloading load under lateral contact by introducing rigorous boundary conditions and a continuity correction factor.

4.1 Physical Assumptions of the Unloading Path

To theoretically characterize the complex unloading behavior, this paper introduces the classic unloading assumption proposed by Thornton and Ning [48]: regardless of the degree of plastic flow experienced during the loading stage, the unloading process of an asperity starting from any elastoplastic state is considered a purely elastic process. Based on this assumption, the unloading curve can be described by the classic Hertz elastic contact theory. However, during the unloading process, the asperity undergoes permanent plastic "flattening," and its geometric shape is no longer the original paraboloid but is equivalent to an elastic body with a new radius of curvature (denoted as $R_{\mathrm{m}}^{'}$). Furthermore, the unloading curve does not return to the origin but terminates at the residual deformation point ω_{res} when the load is zero.

If the maximum loading point is in the fully elastic stage ($\omega_{\max}<\omega_1$), the unloading path completely overlaps with the loading path ($\omega_{\mathrm{res}}=0$); if the maximum loading point is in the fully plastic stage, the deformation is irreversible and the unloading load drops rapidly to zero. This derivation focuses on unloading from the elastoplastic state most

common in engineering ($\omega_1 < \omega_{max} < \omega_2$). To establish this Hertz unloading curve, the core premise is that the residual deformation ω_{res} must be accurately obtained first.

4.2 Finite Element Empirical Model for Residual Deformation of Elliptical Paraboloids

Classic empirical residual deformation models (such as the KE model [25] established by Etsion et al.) have been widely used in tribological research. However, the KE model is strictly limited to isotropic hemispherical asperity geometry, and its validated application range is usually limited to $1 < \omega_{max}/\omega_1 < 150$. For anisotropic elliptical paraboloids, there is currently a lack of a residual deformation calculation model that includes asperity morphology parameters.

To this end, this paper defines the shape parameter of the asperity as $\lambda = R_x/R_y$ (the ratio of two orthogonal principal radii of curvature; when λ=1, it degenerates into a rotational paraboloid). Based on this, 10 sets of finite element contact simulation experiments covering different material properties (AISI 45 steel and 2A12 aluminum alloy) and shape parameters (λ between 1 and 9) were designed (see Table 1 for parameter configuration).

Table 1. Materials and geometrical properties combinations

Case	E/GPa	R_{el}	ν	λ	R_m/mm
1	210	400	0.3	1	6.25
2				3	6.25
3				5	4.1667
4				7	3.125
5				9	2.5
6	70	300	0.32	1	6.25
7				3	6.25
8				5	4.1667
9				7	3.125
10				9	2.5

A finite element model was established, as illustrated in Fig. 5 Both asperities were modeled using SOLID186 elements. During meshing, local mesh refinement was applied to the regions in the vicinity of the contact interface. The total number of elements ranged from approximately 80,000 to 120,000, with the exact number varying slightly depending on the asperity geometry. The bottom surface of the lower asperity

was fully constrained, while a prescribed downward displacement of varying magnitude was applied to the bottom surface of the upper asperity and subsequently unloaded. The maximum deformation considered in the analysis was set to $300\omega_1$, which exceeds the limit of $150\omega_1$ adopted in the KE model [25], thereby extending the applicable range of the proposed model. During the unloading process, the residual deformation ω_{res} was determined by extracting the displacement corresponding to zero reaction force within the contact region.

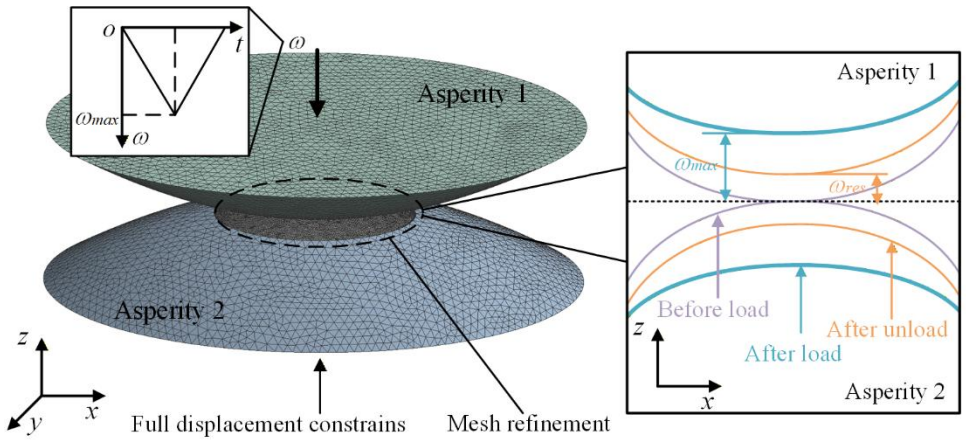


Fig. 5. Finite element simulation model for obtaining residual deformation

Fig. 6 plots the evolution curves of the dimensionless residual deformation ratio ($\omega_{res}/\omega_{max}$) with the dimensionless maximum load (ω_{max}/ω_1) for two materials under different λ values. It can be observed that at the same dimensionless loading level, the curves corresponding to different shape parameters λ show obvious systematic separation, which directly proves that anisotropic geometry has a non-negligible physical impact on residual deformation.

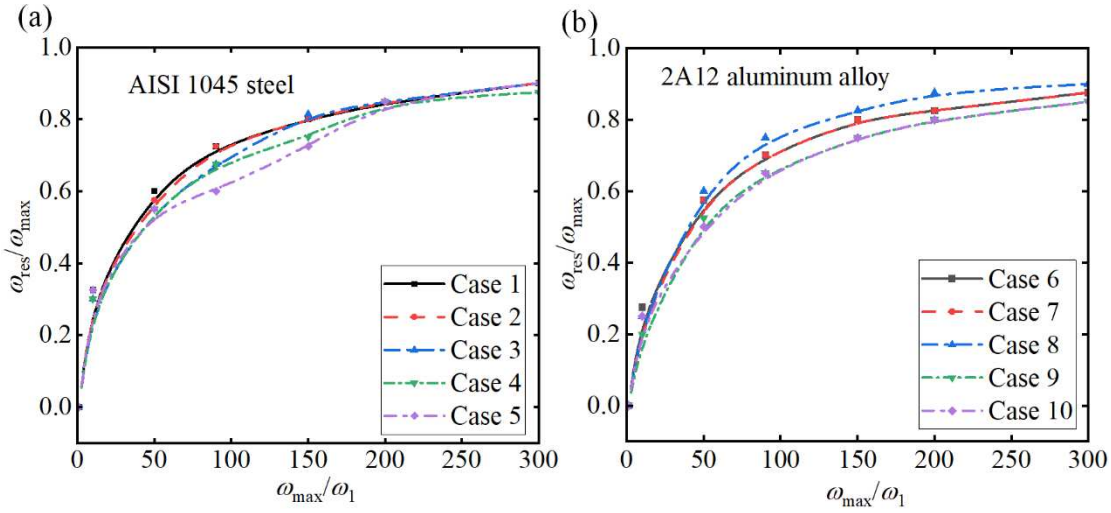


Fig. 6. Simulation results of the relationship between the normalized residual

deformation and the maximum loading: (a) micro-asperity made of AISI 1045 steel, (b) micro-asperity made of 2A12 aluminum alloy.

To theorize this rule, this paper follows the basic structure of the power function from the classic literature [25], but innovatively converts its coefficients into a function of the shape parameter λ:

$$\omega_{res} = \omega_{max} \frac{\left(\omega_{max} / \delta_1 \cos\theta\right)^{A(\lambda)} - 1}{\left(\omega_{max} / \delta_1 \cos\theta\right)^{A(\lambda)} + B(\lambda)} \tag{15}$$

Using the least-squares method to perform regression analysis on each set of simulation data, the saturation upper limit coefficient A and the transition rate coefficient B were extracted. Further fitting shows that $A(\lambda)$ and $B(\lambda)$ follow a Lorentz-type function distribution, as shown in Fig. 7.

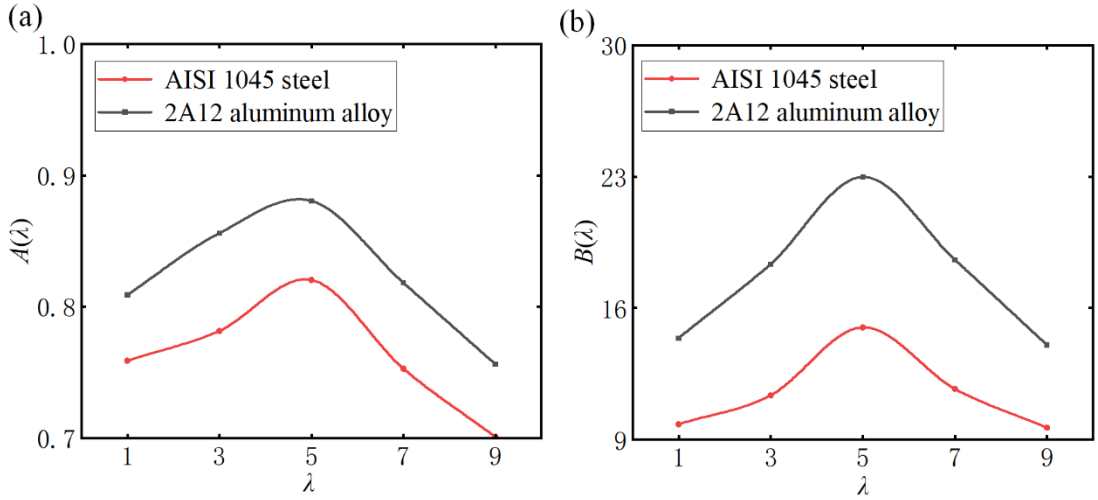


Fig. 7. Relationships between the fitting parameters A and B and λ: (a) parameter A, (b) parameter B.

The paper provides the specific Lorentz parameters for 45 steel and 2A12 aluminum alloy:

$$\begin{aligned} A_{steel}(\lambda) &= 0.556 + \frac{0.254}{1 + \left(\frac{\lambda - 4.17}{5.65}\right)^2} \qquad (1 \le \lambda \le 9) \\ B_{steel}(\lambda) &= 8.616 + \frac{6.375}{1 + \left(\frac{\lambda - 5.07}{1.83}\right)^2} \qquad (1 \le \lambda \le 9) \end{aligned} \tag{16}$$

$$A_{al}(\lambda)=0.612+\frac{0.267}{1+\left(\frac{\lambda-4.25}{5.2}\right)^2}\qquad(1\le\lambda\le9)$$
$$B_{al}(\lambda)=10.249+\frac{12.735}{1+\left(\frac{\lambda-5.01}{2.69}\right)^2}\qquad(1\le\lambda\le9)\tag{17}$$

4.3 Theoretical Derivation of Simplified Unloading Loads

After obtaining reliable ω_{res}, this paper combines the aforementioned pure elastic unloading assumption to derive the functional relationship between unloading load and displacement.

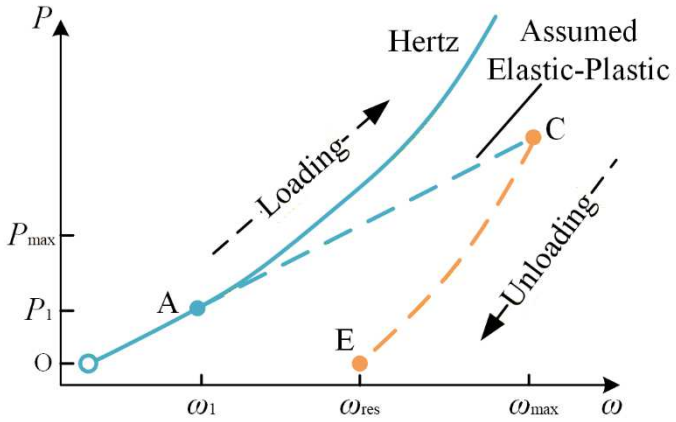


Fig. 8. Schematic illustration of the simplified linear loading path (O-A-C) and the unloading path (C-E) used for deriving the unloading curvature.

As shown in Fig. 8, to solve for algebraic closure, a simplified linear loading imaginary path (along the O-A-C segment in the figure) is first introduced. Assume that after passing the elastic critical point A, the asperity no longer exhibits true elastoplastic non-linearity but presents a linear loading response until reaching the imaginary maximum deformation point C (ω_{max}, $P_{ul,max}$).Starting from point C and unloading to the residual deformation point E (ω_{res}, 0), since the process is purely elastic, its load $P_{ul}(\omega)$ strictly follows the Hertz relationship with an unknown equivalent radius of curvature $R_m^{'}$:

$$P_{ul}=\frac{4\sqrt{2}}{3}ER_m'^{0.5}\left(\frac{\omega-\omega_{res}}{\gamma}\right)^{1.5}\tag{18}$$

4.4 Continuity Correction and Closed-Form Solution for Elastoplastic Non-linearity

Directly using the formula from Section 4.3 to describe unloading has a significant

physical flaw: the true elastoplastic loading curve (the O-D path in Fig. 9) is highly non-linear. At the maximum loading displacement ω_{max}, the true elastoplastic contact load P_{max} (provided by the loading model in Section 3) is not equal to the imaginary linear load $P_{ul,max}$. If one unloads directly from the imaginary point C, the load will experience an unphysical "jump" at the maximum contact point, violating the principle of continuity in mechanical evolution.

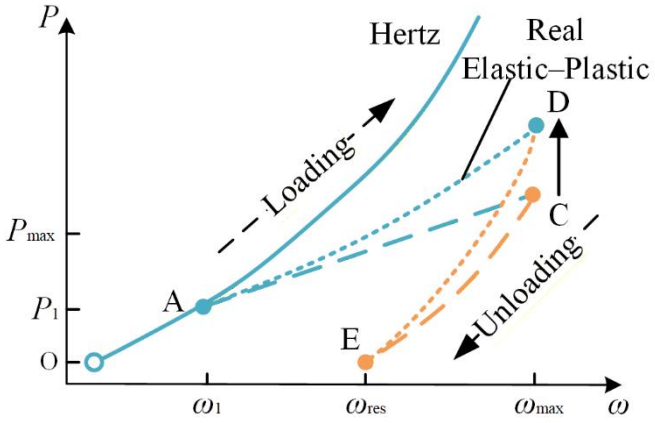


Fig. 9. Schematic illustration of the actual elastoplastic loading path (O-D) and the corrected unloading path (D-E) with the introduction of the continuity-preserving correction factor m.

To eliminate this discontinuity, this paper introduces a dimensionless continuity correction factor m, defined as the ratio of the true elastoplastic load to the imaginary linear load:

$$m = \frac{P_{max}}{P_{ul,max}} \tag{19}$$

The correction factor m has a clear physical meaning: it essentially compensates mathematically for the "geometric hardening effect caused by asperity plastic flow" that is ignored due to the simplified linear assumption. To ensure the unloading curve can smoothly depart from the true loading end point D(ω_{max},P_{max}) while still ensuring the unloading end point falls precisely on the theoretically evaluated residual deformation point E(ω_{res},0), the only path is to perform scaling correction on the equivalent curvature of the unloading system.

We let the true unloading equivalent curvature $R_{mp}=m^2R_m^{'}$. Based on the assumption of Thornton and Ning [40], the entire pure elastic unloading process can be completely characterized by this single equivalent curvature. Therefore, this correction not only

ensures first-order continuity at the maximum load point but is also strictly valid at any unloading displacement ω.

Based on the physical mechanisms above, the closed-form solution for lateral elastoplastic unloading loads derived in this paper, which possesses high physical consistency, is finally expressed as:

$$P_{\mathrm{ul}}=\frac{4\sqrt{2}}{3}ER_{\mathrm{mp}}^{0.5}\left(\frac{\delta\cos\theta-\delta_{\mathrm{res}}\cos\theta}{\gamma}\right)^{1.5} \tag{20}$$

5 Finite Element Validation and Discussion

5.1 Finite Element Validation of Contact Mechanical Response

Based on Abaqus commercial software, a parameterized finite element model for lateral contact was built. As shown in Fig. 10, the model consists of two opposing elliptical paraboloid asperities. The bottom of the lower asperity is fully constrained, while the upper asperity is set with an initial tangential offset (r_x, r_y) in the horizontal direction, followed by a displacement load applied along the normal of the contact surface. To accurately capture the high-gradient stress and large deformation features of the contact interface, the mesh in the contact region was locally highly refined using C3D10 ten-node quadratic tetrahedral elements, with a total system element count of approximately 90,000. Typical engineering materials were selected for the model: AISI 45 steel (E=210 GPa, ν=0.30, σ_y=400 MPa), and the material constitutive models were both set as isotropic hardening elastoplastic models following the Von Mises yield criterion.

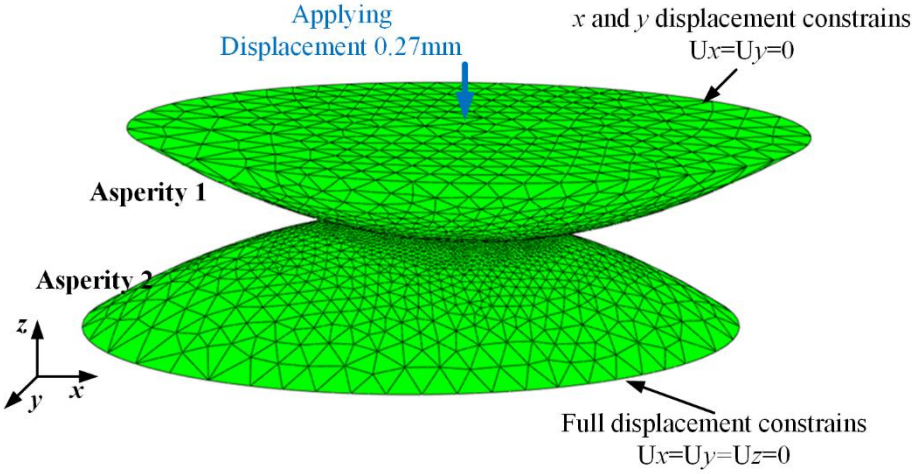


Fig. 10. Finite element model.

To comprehensively evaluate the prediction accuracy of the analytical model, this paper examines a base case including initial offsets (morphology parameters a=0.05,

b=0.02, and c_1= c_2=5, tangential offset r_x=r_y=2 mm). The normal loading process was discretized into 10 increment steps (maximum normal displacement 0.27 mm), followed by complete unloading. Note that for the convenience of FE meshing and calculation, the FE geometric model used macroscopic proportional scaling (mm level); since contact mechanics satisfy geometric similarity laws, this does not affect the universality of the dimensionless results. The results are shown in Fig. 11.(a); the loading contact area predicted by this model is in high agreement with the FE simulation results, with a maximum relative error of only 9.18%. Regarding the validation of elastoplastic loading-unloading loads, as shown in Fig. 11.(b), the model not only precisely tracked the loading path (maximum error 8.08%) but also maintained high consistency with simulation data for the unloading paths under three different maximum loading levels, with the maximum error for the unloading process strictly controlled within 10%.

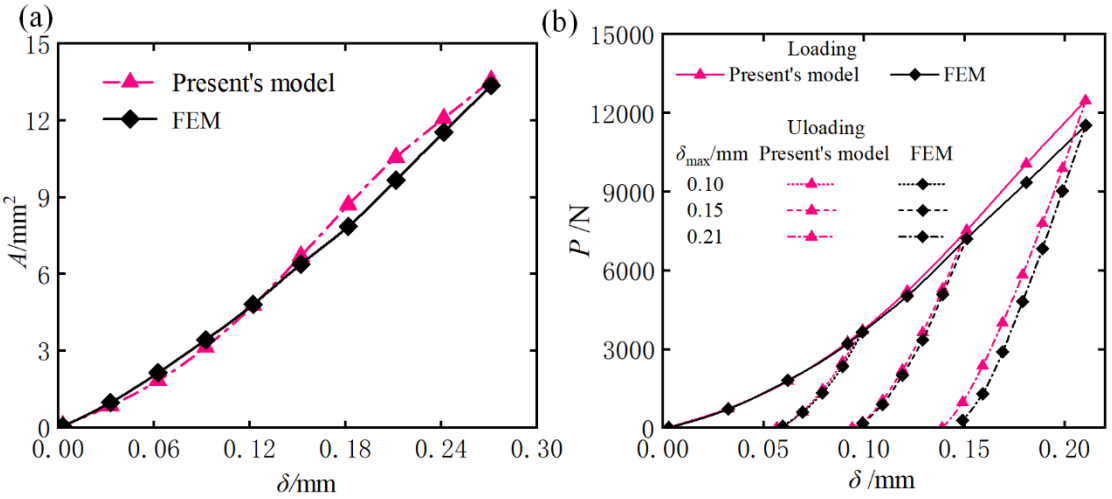


Fig. 11. (a) Contact area validation during the loading process. (b) Finite element validation of contact load curve during loading and unloading.

The results show that the model has good convergence for the prediction errors of contact area and loading-unloading loads. Although direct nano-indentation experiments were not conducted due to equipment limitations, the robustness and engineering applicability of this closed-form analytical model have been fully demonstrated based on 3D elastoplastic FE validation with rigorous mesh sensitivity checks (which already constitutes a recognized reliable verification paradigm in single-peak contact theory research [25, 34, 40]).

5.2 Comparative Discussion with Existing Spherical Contact Models

To highlight the uniqueness of anisotropic lateral contact mechanical behavior, this paper compares the results of the established model with classic hemispherical against rigid-plane normal contact models in the literature (including SK, LL, ZZ, ZNZ, EKK, JG, etc. [16, 25, 26, 35, 49, 50]).

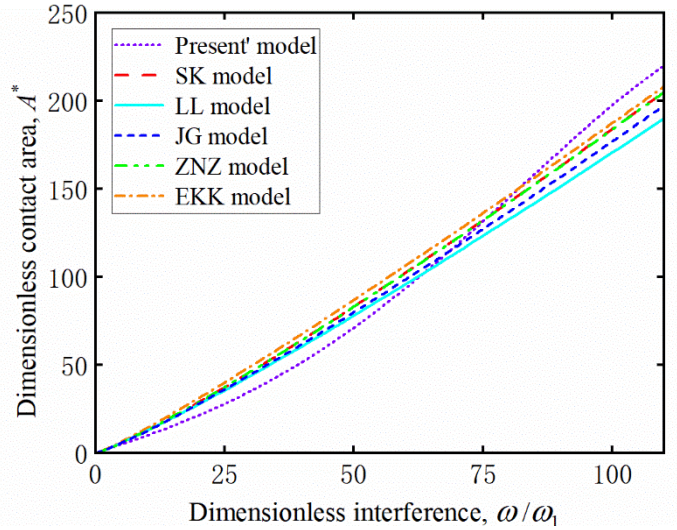


Fig. 12. Comparison of contact area predictions obtained from different models

Fig. 12 shows the predicted trajectories of contact area by different models. It can be observed that under the same dimensionless interference, the prediction curves of classic spherical models such as SK, ZNZ, and EKK are highly coincident, while the model in this paper predicts significantly lower area values near $\omega\approx35\omega_1$ compared to these classic models, but presents a higher growth rate in the extreme deformation zone ($\omega\approx100\omega_1$).

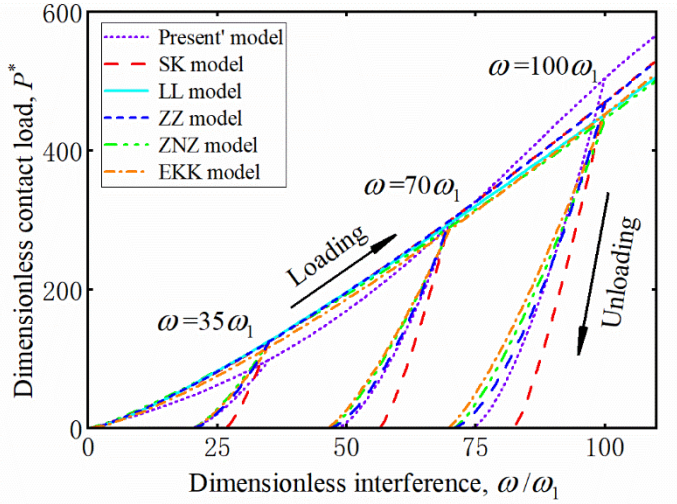


Fig. 13. Comparison of contact load predictions obtained from different models

Similarly, Fig. 13 compares the contact load response of different models throughout the entire loading-unloading cycle. In the loading stage, the slope of the load

curve of this model differs significantly from the various spherical models; whereas in the unloading stage, due to the different assessment mechanisms for residual deformation, the unloading path predicted by this paper also has a unique morphology.

It must be emphasized that the significant difference in prediction results does not originate from evaluation errors in this model, but because there is a fundamental difference in the underlying physical contact configuration. This model characterizes the spatial coupling contact of two anisotropic elliptical paraboloids under tangential offset, while existing models are limited to the pure normal compression of axisymmetrical hemispheres. This sharp contrast profoundly reveals that when dealing with contact mechanics problems on real machined surfaces, if existing spherical normal contact models are forced upon them, it will lead to non-negligible theoretical deviations in the assessment of contact area and contact stiffness because the anisotropy of microscopic geometry and tangential offset mechanisms are ignored.

5.3 Coupling Effect of Geometric Morphology and Tangential Offset

To clarify the regulatory mechanism of asperity anisotropy on its loading-unloading contact characteristics, this paper defines the morphology parameter $\lambda=R_x/R_y$ (numerically equivalent to the ratio of the original equation coefficients b/a).

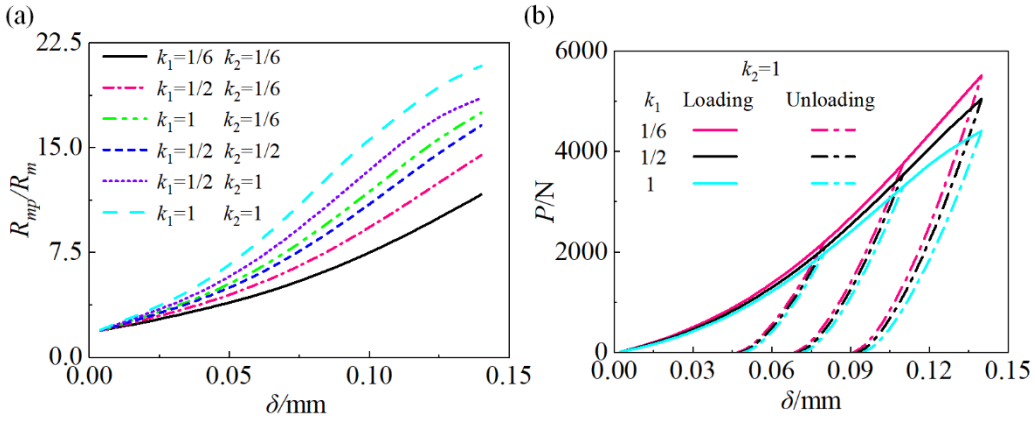


Fig. 14. Influence of ellipticity and interference on the contact characteristics: (a) unloading equivalent radius of curvature (b) contact load curve

Fig. 14 comprehensively demonstrates the effect of morphology parameters on the correction of the unloading equivalent radius of curvature and the influence on loading-unloading loads. On one hand, under the same maximum interference, as the degree of asperity anisotropy intensifies (i.e., the parameter gap widens), the ratio of the unloading equivalent radius of curvature to the radius during loading shows a significant increasing trend. This indicates that the geometric recovery of elongated

asperities during unloading exhibits stronger asymmetry, leading to a sharp increase in the magnitude of the equivalent curvature correction introduced to maintain physical boundary continuity. On the other hand, from the load curve perspective, the larger the morphology coefficient of the asperity (the more significant the anisotropy), the higher the macroscopic contact force triggered under the same normal loading displacement.

In addition to the asperity's own anisotropy, spatial tangential offset also fundamentally changes the local stiffness of the contact interface. To reveal this complex spatial coupling behavior panoramically, Fig. 15 plots a 3D parameter response surface including contact load, tangential offset, and normal loading-unloading displacement.

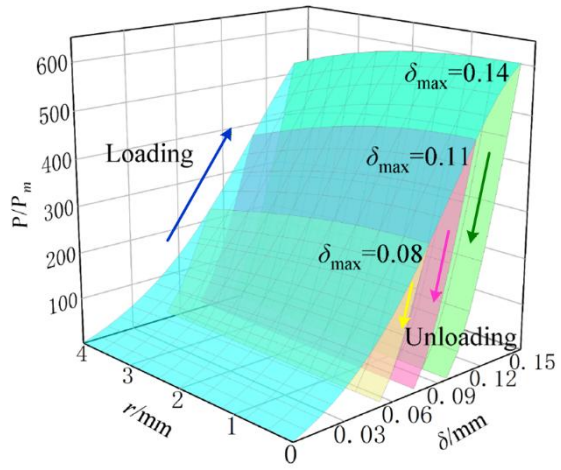


Fig. 15. Relationship among load, offset, and loading-unloading displacement.

From this 3D response surface, it can be clearly observed that for anisotropic elliptical paraboloid contact, the contact load produced at the same normal displacement decreases monotonically as the tangential offset increases. This "stiffness softening effect" induced by the spatial misalignment of anisotropic principal axes does not exist only at a specific moment but runs through the entire loading-unloading cycle of the asperity. More critically, as the normal displacement increases (i.e., the asperity enters deeper elastoplastic and fully plastic deformation stages), the load attenuation caused by tangential offset increases, causing the 3D load surface to exhibit a characteristically steep landslide morphology in the deep loading zone. This phenomenon fully proves that when establishing high-fidelity macroscopic contact models for rough surfaces, the tangential offset between asperities must be included as a core variable.

5.4 Evolution Mechanism of Material Properties and Contact Stress Field

To explore the influence of material constitutive differences on contact mechanical response, this section uses the two typical material parameters set in Section 4.2 (Table 1). Under the same anisotropic geometric morphology and loading conditions, Fig. 16 visually compares the elastoplastic contact response of 45 steel (Case 2) and 2A12 aluminum alloy (Case 7) asperities. The results show that because 45 steel has a higher elastic modulus and initial yield strength, the maximum equivalent stress excited at the contact interface (approx. 414 MPa) is significantly higher than that of 2A12 aluminum alloy (approx. 307 MPa). From the displacement deformation cloud maps, it can be observed that although the plastic deformation zones of both materials expand into the material matrix in an approximately semi-ellipsoidal shape, affected by the combined effects of the two materials' yield strength and strain hardening characteristics, AISI 45 steel produces a more significant irreversible plastic deformation volume under the same loading displacement.

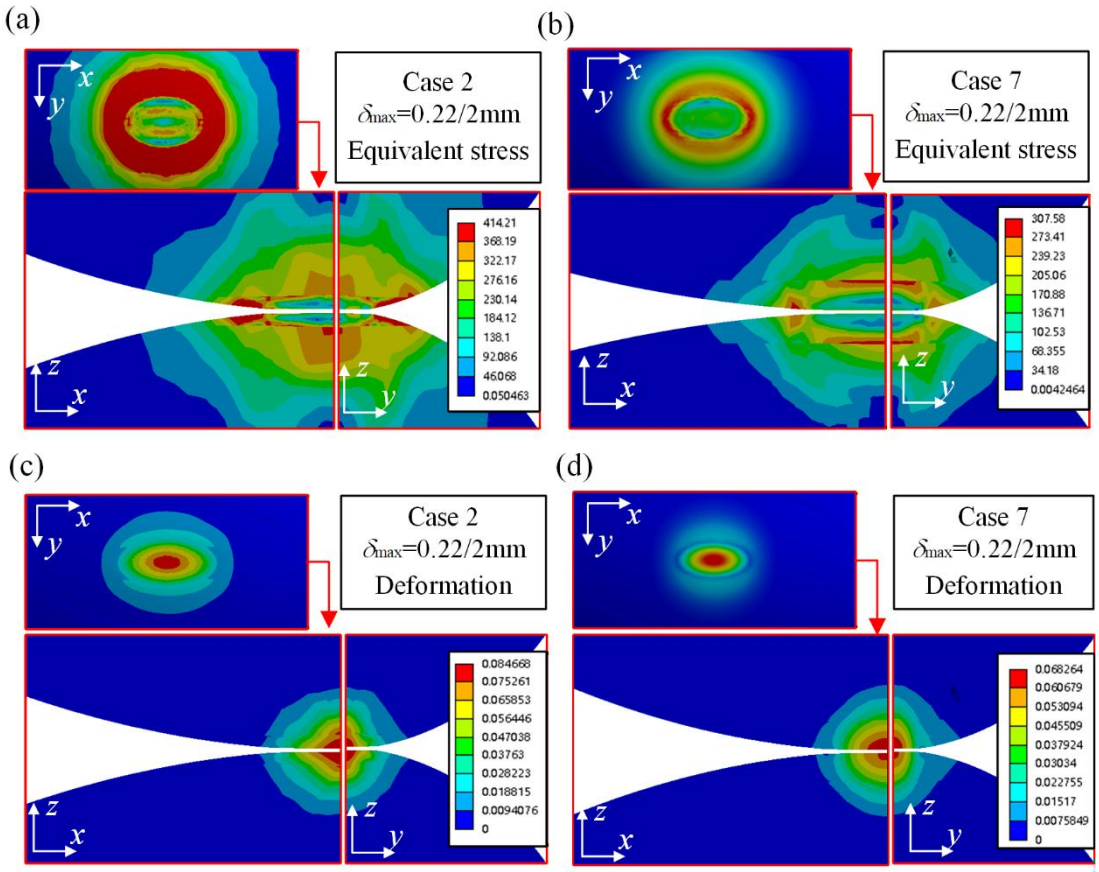


Fig. 16. Simulation contour plots of asperities with different materials: (a)Equivalent stress of case 2 (b) Equivalent stress of case 7 (c) Deformation of case 2 (d) Deformation of case 7.

To profoundly reveal the underlying regulatory mechanism of anisotropic

morphology on the evolution law of the internal stress field of asperities, this paper further compares the stress states of a rotational paraboloid and an elliptical paraboloid with the same equivalent radius of curvature under the same maximum loading.

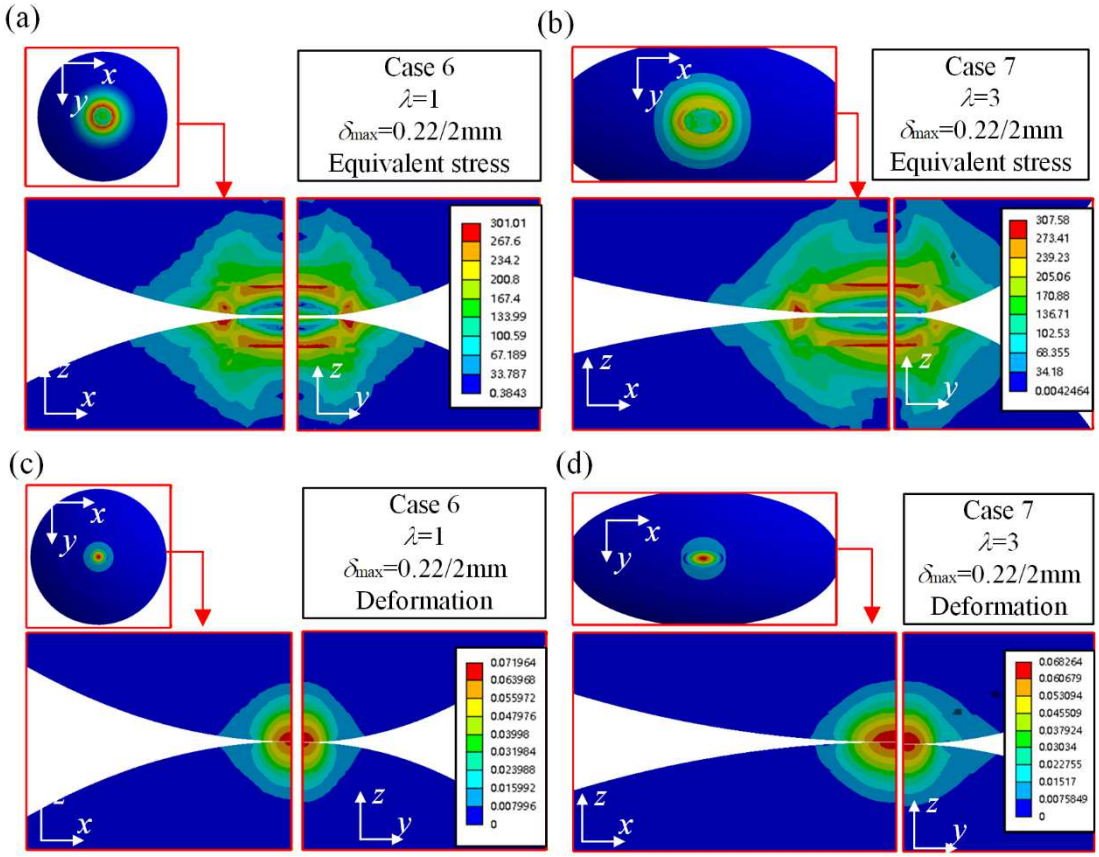


Fig. 17. Comparison of simulation results between rotational paraboloid and elliptic–paraboloid asperities: (a) Equivalent stress of case 6 (b) Equivalent stress of case 7 (c) Deformation of case 6 (d) Deformation of case 7.

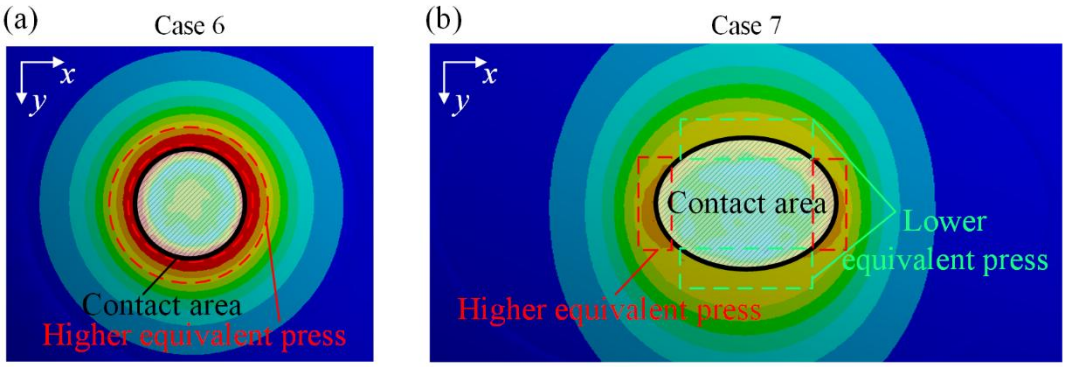


Fig. 18. Stress distribution in the contact region: (a) Rotational paraboloid (b) Elliptical paraboloid asperities.

Fig. 17 and Fig. 18 detail the micro-stress distribution features of the contact region. Simulation results confirm that regardless of the asperity shape, plastic yielding always

originates at the outer boundary of the contact region. However, due to the spatial asymmetry of geometric curvature, the stress field morphology of the two shows essential differences. For the classic rotational paraboloid, its contact boundary forms a circular high-stress ring with a uniform stress distribution; while for the elliptical paraboloid, the contact surface evolves into a typical elliptical ring-shaped anisotropic stress concentration zone.

Combining the stress distribution at the contact boundary, it can be clearly found that the equivalent stress of the elliptical paraboloid is not uniformly distributed along the circumference; its highest stress is fixedly concentrated near the two ends (poles) of the major axis of the contact ellipse, while the stress level in the edge regions of the minor axis shows a significant drop. Analyzing from the perspective of solid mechanics and plastic dissipation, this non-uniform stress gradient along the contact boundary produces a unique physical effect: the low-stress zones at the two ends of the minor axis physically act as "plastic suppression zones," effectively hindering the violent expansion of plastic deformation toward that transverse dimension.

It is precisely because of the suppression effect of this local low-stress region that under the exact same macroscopic normal loading displacement, the depth of plastic deformation accumulated inside the highly anisotropic elliptical paraboloid is slightly lower than that of the isotropically rotational symmetric asperity. This micro-mechanical mechanism fundamentally explains why the morphology parameter (λ) of an asperity can significantly change the unloading residual deformation of a system, and further confirms the absolute necessity of introducing anisotropic geometric representation in contact mechanics models.

6 Conclusions

Based on real surface morphology statistics and 3D finite element simulation, this paper establishes a lateral anisotropic elastoplastic loading-unloading contact mechanics model that includes shape parameters and tangential offset effects. The main conclusions are as follows:

(1) Three-dimensional topography measurements of ground, milled, and turned AISI 1045 steel surfaces, analyzed via watershed segmentation, statistically confirm that the elliptical paraboloid significantly outperforms the classical rotational paraboloid in representing real asperity geometry, thereby substantiating the geometric foundation of the proposed contact model.

(2) An empirical residual deformation model incorporating the shape parameter $\lambda=R_x/R_y$ is established based on comprehensive FE simulations covering multiple materials and ellipticities. This model extends the classical KE unloading theory from spherical to elliptical paraboloidal geometries and expands the applicable loading range from $150\omega_1$ to $300\omega_1$.

(3) A closed-form elastoplastic unloading solution for lateral contact is derived. By introducing a continuity-preserving correction factor m, the geometric hardening induced by plastic flow is mathematically compensated, yielding explicit unloading load expressions that maintain strict boundary continuity throughout the loading-unloading cycle. The proposed model is validated against FE simulations with a maximum error below 10%.

(4) Parametric analysis reveals that tangential offset continuously modulates the contact stiffness throughout the loading-unloading cycle. For elliptical paraboloidal asperities, increasing tangential offset induces a distinct stiffness softening effect, causing a monotonic decrease in contact load under the same normal displacement.

(5) The elliptical paraboloid generates a unique anisotropic stress concentration at the contact boundary, where the low-stress zones near the minor-axis edges physically suppress the transverse expansion of plastic deformation. This mechanism inherently explains the reduced residual deformation observed in anisotropic contacts.

Statements and Declarations

Funding

This work was supported by the National Natural Science Foundation of China (No. 52335011, No. 52275510), and Fundamental Research Funds for the Central Universities (No. xzy012024084).

Competing Interests

The authors have no relevant financial or non-financial interests to disclose.

Author Contributions

All authors contributed to the study conception and design. Data collection and analysis were performed by Junbing Liu. The first draft of the manuscript was written by Linbo Zhu and Jian Chen. All authors commented on previous versions of the manuscript. All authors read and approved the final manuscript.

Data Availability

All data reported in a graphical format can be requested from the corresponding

author.

References

1. Tiwari, A., Persson, B.N.J.: Cylinder-Flat Contact Mechanics with Surface Roughness. Tribol. Lett. **69**(1) (2021)
2. Yuan, B., Sun, Q.C., Wang, X.X., Mu, X.K., Wang, Y.L., Sun, W.: A novel acoustic model for interface stiffness measurement of dry tribological interface considering geometric dispersion effect and boundary effect. Tribol Int. **162** (2021)
3. Jiang, K., Liu, Z.F., Yang, C.B., Zhang, C.X., Tian, Y., Zhang, T.: Effects of the joint surface considering asperity interaction on the bolted joint performance in the bolt tightening process. Tribol Int. **167** (2022)
4. Zhang, S.Y., Li, D.W., Liu, Y.W.: Friction Behavior of Rough Surfaces on the Basis of Contact Mechanics: A Review and Prospects. Micromachines. **13**(11) (2022)
5. Chen, S.W., Wang, G.F.: A contact model for elastic-plastic rough spheres. Tribol Int. **206** (2025)
6. Gargourimotlagh, M., Matthews, D., de Rooij, M.: An investigation into the evolution of surface topography and contact characteristics of rolling elements under repeated rolling contact. Tribol Int. **208** (2025)
7. Ma, H.L., Zhang, T., Yang, C.B., Liu, Z.F., Cheng, Q., Chen, C.H.: Multi Objective Optimization Research on Power Consumption and Stiffness of Internal Feedback Hydrostatic Turntable. Int. J. Precis. Eng. Manuf.-Green Technol. **12**(4),1261-1276 (2025)
8. Xiang, G., Goltsberg, R., Etsion, I.: Effects of sphere size and fracture parameters on adhesive wear in elastic-plastic spherical microcontacts. Tribol Int. **207** (2025)
9. Zhang, H.B., Liu, S.L., Wang, W.Z.: Generation of non-Gaussian rough surfaces based on fractal theory and genetic algorithm. Tribol Int. **205** (2025)
10. Zhao, B.B., Mu, X.K., Li, H., Du, W.L., Sun, Q.C.: A novel intelligent assembly-adjustment method for aero-engine rotor system aimed at improving interface load-bearing performance. J. Manuf. Syst. **80**,126-139 (2025)
11. Zhao, H., Huang, D.F., Ta, W., Zhou, Y.H.: Reconstruction and prediction of opaque rough surface morphology based on friction force evolution. Tribol Int. **206** (2025)
12. Greenwood, J.A., Williamson, J.B.: Contact of nominally flat surfaces. Proc. R. Soc. Lond. A. **295**(1442),300-+ (1966)
13. Chang, W.R., Etsion, I., Bogy, D.B.: An elastic-plastic model for the contact of rough surfaces. J. Tribol. **109**(2),257-263 (1987)
14. Zhao, Y.W., Maietta, D.M., Chang, L.: An asperity microcontact model incorporating the transition from elastic deformation to fully plastic flow. J. Tribol. **122**(1),86-93 (2000)
15. Kogut, L., Etsion, I.: Elastic-plastic contact analysis of a sphere and a rigid flat. J. Appl. Mech. **69**(5),657-662 (2002)
16. Jackson, R.L., Green, I.: A finite element study of elasto-plastic hemispherical contact against a rigid flat. J. Tribol. **127**(2),343-354 (2005)
17. Lamura, M.D.P., Hidayat, T., Ammarullah, M.I., Bayuseno, A.P., Jamari, J.: Study of contact mechanics between two brass solids in various diameter ratios and friction coefficient. Proc. Inst. Mech. Eng. Part J-J. Eng. Tribol. **237**(8),1613-1619 (2023)

18. You, S.Y., Tang, J.Y.: A New Model for Sphere Asperity Contact Analysis Considering Strain Hardening of Materials. Tribol. Lett. **70**(4) (2022)
19. Zhang, W.Y., Chen, J., Wang, C.L., Liu, D., Zhu, L.B.: Research on Elastic-Plastic Contact Behavior of Hemisphere Flattened by a Rigid Flat. Materials. **15**(13) (2022)
20. Edmans, B.D., Sinka, I.C.: Unloading of elastoplastic spheres from large deformations. Powder Technol. **374**,618-631 (2020)
21. Weng, P.P., Yin, X.C., Hu, W., Yuan, H., Chen, C.Q., Ding, H.P., Yu, B., Xie, W.H., Jiang, L., Wang, H.: Piecewise linear deformation characteristics and a contact model for elastic-plastic indentation considering indenter elasticity. Tribol Int. **162** (2021)
22. Lontin, K., Khan, M.: Interdependence of friction, wear, and noise: A review. Friction. **9**(6),1319-1345 (2021)
23. Chen, J., Zhang, W.Y., Wang, C.L., Liu, D., Zhu, L.B.: Effect of Strain Hardening and Ellipticity on Elastic-Plastic Contact Behaviour between Ellipsoids and Rigid Planes. Machines. **10**(6) (2022)
24. Vu-Quoc, L., Zhang, X., Lesburg, L.: A normal force-displacement model for contacting spheres accounting for plastic deformation: Force-driven formulation. J. Appl. Mech.. **67**(2),363-371 (2000)
25. Etsion, I., Kligerman, Y., Kadin, Y.: Unloading of an elastic-plastic loaded spherical contact. Int J Solids Struct. **42**(13),3716-3729 (2005)
26. Zhao, J.H., Nagao, S., Zhang, Z.L.: Loading and unloading of a spherical contact: From elastic to elastic-perfectly plastic materials. Int. J. Mech. Sci. **56**(1),70-76 (2012)
27. Chen, C.Q., Wang, Q., Wang, H., Ding, H.P., Hu, W., Xie, W.H., Weng, P.P., Jiang, L., Yin, X.C.: Contact Unloading Behaviors of Elastic-Power-Law Strain Hardening Material Considering Indenter Elasticity Effect. J. Tribol. **144**(12) (2022)
28. Luo, J.C., Liu, J.H., Xia, H.X., Ao, X.H., Zhang, J., Zhang, X.R., Zhang, H., Liu, X.: A numerical study of the normal loading-unloading contact behaviors considering yield plateau and strain hardening. Arch. Appl. Mech. **95**(2) (2025)
29. Chen, J., Zhang, W.Y., Wang, C.L., Liu, D., Zhu, L.B.: An accurate solution of a hemisphere contact against a rigid flat under varying elastic moduli and yield strengths and comparison with previous model. J. Mech. Sci. Technol. **36**(9),4615-4624 (2022)
30. Li, X.Y., Liang, L., Wu, S.J.: A numerical and effective method for the contact stress calculation of elliptical partial slip. J. Mech. Sci. Technol. **29**(2),517-525 (2015)
31. Horng, J.H.: An elliptic elastic-plastic asperity microcontact model for rough surfaces. J. Tribol. **120**(1),82-88 (1998)
32. Wen, Y.Q., Tang, J.Y., Zhou, W., Zhu, C.C.: A new elliptical microcontact model considering elastoplastic deformation. Proc. Inst. Mech. Eng. Part J-J. Eng. Tribol. **232**(11),1352-1364 (2018)
33. Bush, A.W., Gibson, R.D., Keogh, G.P.: Strongly anisotropic rough surfaces J. Lubr. Technol. **101**(1),15-20 (1979)
34. Jamari, J., Schipper, D.J.: An elastic-plastic contact model of ellipsoid bodies. Tribol. Lett. **21**(3),262-271 (2006)
35. Lin, L.P., Lin, J.F.: An elliptical elastic-plastic microcontact model developed for an ellipsoid in contact with a smooth rigid flat. J. Tribol. **129**(4),772-782 (2007)
36. Zhang, W.Y., Chen, J., Wang, C.L., Liu, D., Zhu, L.B.: Analysis of Elastic-Plastic Loading and Unloading Contact between Ellipsoid and Rigid Flat. Proc. Inst. Mech. Eng. Part J-J. Eng. Tribol. **237**(3),541-551 (2023)

37. Chen, J., Zhang, W.Y., Liu, D., Wang, C.L., Zhu, L.B.: Loading-unloading model of contact between elastic-plastic ellipsoid and rigid plane. J. Mech. Sci. Technol. **37**(8),4159-4168 (2023)
38. Wen, Y.Q., Tang, J.Y., Zhou, W., Li, L., Zhu, C.C.: New analytical model of elastic-plastic contact for three-dimensional rough surfaces considering interaction of asperities. Friction. **10**(2),217-231 (2022)
39. Wen, Y.Q., Tang, J.Y., Zhou, W., Li, L.: A Reconstruction and Contact Analysis Method of Three-Dimensional Rough Surface Based on Ellipsoidal Asperity. J. Tribol. **142**(4) (2020)
40. Becker, V., Kamlah, M.: A theoretical model for the normal contact force of two elastoplastic ellipsoidal bodies. J. Appl. Mech. **88**(3) (2021)
41. Peng, J.F., Hong, J., Zhuang, Y.: A New Model for Constriction Resistance of Rough Contacts between Nominally Flat Surfaces. 2nd Int. Conf. Mech. Aerosp. Eng. (ICMAE 2011), pp. 977-984. Place (2011)
42. Zhou, C.J., Huang, F.T., Han, X., Gu, Y.T.: An elastic-plastic asperity contact model and its application for micro-contact analysis of gear tooth profiles. International Int. J. Mech. Mater. Des. **13**(3),335-345 (2017)
43. Wang, S.J., Fan, L.S., Wu, J.W., Li, P.Y.: A Side Contact Model of Joint Considering the Horizontal Distance Distribution Between Asperities. J. Tribol. **144**(10) (2022)
44. Mezghani, S., Zahouani, H.: Characterisation of the 3D waviness and roughness motifs. Wear. **257**(12),1250-1256 (2004)
45. Barré, F., Lopez, J.: Watershed lines and catchment basins: a new 3D-motif method. Int. J. Mach. Tools Manuf. **40**(8),1171-1184 (2000)
46. Vincent, L., Soille, P.: Watersheds in digital spaces-an efficient algorithm based on immersion simulations. IEEE Trans. Pattern Anal. Mach. Intell. **13**(6),583-598 (1991)
47. Lin, Y.C., Tsai, Y.P., Hung, Y.P., Shih, Z.C.: Comparison between immersion-based and toboggan-based watershed image segmentation. IEEE Trans. Image Process. **15**(3),632-640 (2006)
48. Thornton, C., Ning, Z.M.: A theoretical model for the stick/bounce behaviour of adhesive, elastic-plastic spheres. Powder Technol. **99**(2),154-162 (1998)
49. Song, Z., Komvopoulos, K.: An elastic-plastic analysis of spherical indentation: Constitutive equations for single-indentation unloading and development of plasticity due to repeated indentation. Mech. Mater. **76**,93-101 (2014)
50. Zhao, B., Zhang, S., Wang, P., Hai, Y.: Loading-unloading normal stiffness model for power-law hardening surfaces considering actual surface topography. Tribol Int. **90**,332-342 (2015)

Appendix A. Derivation of Contact Point Coordinates and Equivalent Curvature Radius

This appendix provides the detailed algebraic derivation of the contact point coordinates, the contact normal vector, the principal curvatures, and the equivalent radius of curvature for two laterally contacting elliptical paraboloidal asperities. The results are essential for establishing the contact framework in Section 3.

A.1 Contact Point Coordinates

Consider two elliptical paraboloidal asperities with surface equations expressed in a unified local coordinate system. At the contact point, the heights of the two surfaces are equal, i.e., z_1=z_2. Substituting the surface equations and rearranging yields:

$$(a_2 - a_1)x^2 + (b_2 - b_1)y^2 + 2a_1 r_x x + 2b_1 r_y y + (c_1' - c_2 - a_1 r_x^2 - b_1 r_y^2) = 0 \qquad \text{(A-1)}$$

This equation represents an ellipse in the xy-plane, confirming that the contact region is elliptical.

Representing the expression in a quadratic form, we obtain:

$$x^T D x + d^T x + c' = 0 \qquad \text{(A-2)}$$

Using the determinant method, the contact point coordinates x_c and y_c are determined as follows:

$$\mathrm{D}_1 = \begin{bmatrix} d_1 & D_{12} \\ d_2 & D_{22} \end{bmatrix} \quad \mathrm{D}_2 = \begin{bmatrix} D_{11} & d_1 \\ D_{21} & d_2 \end{bmatrix} \qquad \text{(A-3)}$$

$$x_c = \frac{\det(D_1)}{\det(D)} \quad y_c = \frac{\det(D_2)}{\det(D)} \qquad \text{(A-4)}$$

A.2 Surface Normal Vector at the Contact Point

The surface gradients at the contact point for the upper and lower asperities are given by:

$$\nabla z_1 = \left[-2a_1 x_c + 2a_1 r_x, -2b_1 y_c + 2b_1 r_y, 1\right] \qquad \text{(A-5)}$$

$$\nabla z_2 = \left[-2a_2 x_c, -2b_2 y_c, 1\right] \qquad \text{(A-6)}$$

Thus, the normal vector at the contact point is:

$$n = \frac{\nabla z_2}{\left\|\nabla z_2\right\|} \qquad \text{(A-7)}$$

A.4 Principal Curvatures via the First and Second Fundamental Forms

To obtain the principal curvatures, we construct the parametric representation of each surface. The tangential vectors $r_{1,u}$ and $r_{1,v}$ at the contact point on the upper asperity are given by:

$$\begin{aligned} r_{1,u} &= \left[1, 0, 2a_1 x_c - 2a_1 r_x\right] \\ r_{1,v} &= \left[0, 1, 2b_1 y_c + 2b_1 r_y\right] \end{aligned} \qquad \text{(A-8)}$$

Similarly, the tangential vectors $r_{2,u}$ and $r_{2,v}$ at the contact point on the lower asperity are given by:

$$r_{2,u} = [1, 0, 2a_2 x_c]$$
$$r_{2,v} = [0, 1, 2b_2 y_c] \tag{A-9}$$

The first fundamental form is expressed as:

$$G_i = \begin{bmatrix} \|r_{i,u}\|^2 & r_{i,u} \cdot r_{i,v} \\ r_{i,u} \cdot r_{i,v} & \|r_{i,v}\|^2 \end{bmatrix} \tag{A-10}$$

The second fundamental form is expressed as:

$$L_i = \begin{bmatrix} r_{i,uu} \cdot n & r_{i,uv} \cdot n \\ r_{i,vu} \cdot n & r_{i,vv} \cdot n \end{bmatrix} \tag{A-11}$$

where, $r_{i,uu}$ and $r_{i,vu}$ represent the second-order partial derivatives of $r_{i,u}$ and $r_{i,v}$ with respect to u, respectively, while $r_{i,uv}$ and $r_{i,vv}$ denote the second-order partial derivatives of $r_{i,u}$ and $r_{i,v}$ with respect to v. Consequently, the final principal curvature κ can be obtained by solving the corresponding eigenvalue problem:

$$\kappa_i = eig\left[G_i^{-1} L_i \right] \tag{A-12}$$

A.5 Normal Deformation

When a certain interference δ is generated along the z-axis between the upper and lower asperities, the deformation in the direction of the contact normal ω an be determined from the cosine component:

$$\cos\theta = \frac{1}{\|n\|} \tag{A-13}$$

$$\omega = \delta \cdot \cos\theta \tag{A-14}$$

This completes the derivation of the geometric parameters required for the lateral contact framework in Section 3.